



AIAA 2003-5052

**The Bidirectional Vortex. Part 1:
An Exact Inviscid Solution**

A. B. Vyas and J. Majdalani
Marquette University
Milwaukee, WI 53233

Propulsion Conference and Exhibit
20–23 July 2003
Huntsville, AL

The Bidirectional Vortex. Part 1: An Exact Inviscid Solution

Anand B. Vyas* and Joseph Majdalani†
Marquette University, Milwaukee, WI 53233

and
Martin J. Chiaverini‡
Orbital Technologies Corporation, Madison, WI 53717

In this paper, we derive an exact solution that describes the bulk fluid motion of a bidirectional coaxial vortex appropriate of a liquid propellant combustion chamber. The study is prompted by the need to characterize the flow inside a laboratory-scale thrust chamber. This chamber has the advantage of confining mixing and combustion to an inner vortex tube that remains separated from the chamber walls by an outer stream of swirling, low temperature oxidizer. Our mathematical model is based on steady, rotational, axisymmetric, incompressible, and inviscid flow conditions. In contrast to other studies of columnar vortices (where the axial dependence is ignored), our model accounts for the chamber's finite body length. In fact, it incorporates the proper inlet and head-end flow conditions associated with a bipolar swirl-driven combustor. Based on the exact solution, several important flow attributes are illuminated. Among them is the location of the non-translating vortex layer known as the mantle. This cylindrical layer separates the outer and inner vortex tubes (i.e., the updraft and the downdraft) and is confirmed using computational fluid dynamics and flow visualization.

Nomenclature

a	= chamber radius
A_i	= inlet area
b	= chamber discharge radius
l	= chamber aspect ratio, L/a
\bar{p}	= normalized pressure, $\bar{p}/(\rho U^2)$
\bar{Q}_i	= inlet volumetric flow rate
Q_i	= normalized volumetric flow rate, $\bar{Q}_i/(Ua^2) = \sigma^{-1}$
Re	= injection Reynolds number, Ua/ν
r	= normalized radial coordinate, \bar{r}/a
S	= swirl number, $\pi ab/A_i = \pi\beta\sigma$
\mathbf{u}	= normalized velocity ($\bar{u}_r, \bar{u}_z, \bar{u}_\theta$)/ U
U	= mean inflow velocity, $\bar{u}_\theta(a, L)$
z	= normalized axial coordinate, \bar{z}/a
β	= normalized discharge radius, b/a
κ	= inflow parameter, $Q_i/(2\pi l) = (2\pi\sigma l)^{-1}$
ν	= kinematic viscosity, μ/ρ
ρ	= density
σ	= modified swirl number, $Q_i^{-1} = S/(\pi\beta)$

*Graduate student and Research Associate, Department of Mechanical and Industrial Engineering. Member AIAA.

†Assistant Professor, Department of Mechanical and Industrial Engineering. Member AIAA.

‡Lead Propulsion Engineer. Member AIAA.

Subscripts

i	= inlet property
r	= radial component or partial derivative
z	= axial component or partial derivative
θ	= azimuthal component or partial derivative
$\bar{}$	= overbars denote dimensional variables

I. Introduction

SWIRLING motions have attracted much attention in recent years due to the rich structures that they engender. Their applications have been diversified due to their development at widely dissimilar scales in a variety of phenomenological problems.

At one end of the spectrum, one is concerned with understanding, predicting or controlling the formation of naturally occurring swirl patterns in geophysical phenomena such as whirlpools, tornadoes, dust devils, waterspouts, hurricanes, fire whirls, or cosmic jets (see Penner¹ and König²). At the other end, one is concerned with the deliberate generation of swirl motions in thermal and physical transport applications whose performance is commensurate with the level of mixing, heat transfer, combustion, chemical dispensing, atomization, or filtration.

So far different methods have been employed to trigger swirl in cylindrical or conical chambers using, for example, tangential fluid injection, inlet swirl vanes,

flat or aerodynamically-shaped swirler blades, vortex trippers, twisted tape inserts, propellers, or coiled wires. Among the salient features of the resulting flows one could set apart vortex breakdown, instability, and reversal as mechanisms requiring further exploration.

One of the earliest investigations of columnar vortices may be traced back to the work of Harvey;³ he reported the presence of vortex disruption in rolled up shear layers above highly swept lifting surfaces (e.g., slender delta wings situated at high angles of attack). This breakdown affected the aerodynamic performance curves and exhibited a distinct stagnation point that was followed by a region of flow reversal. Beyond the stagnation point, a dramatic size increase in the vortex core could be noted in addition to flow transition or increased turbulent fluctuations. In fact, two distinct types of breakdown were reported and these were dubbed the spiral S-shape and the bubble B-shape. These two types of disruption modes were sequentially established with successive increases in the Reynolds number and swirl levels; at fixed swirl levels, higher Reynolds numbers caused the breakdown to move further upstream. A third type of breakdown, the double helix, was discovered by Sarpkaya⁴ at low Reynolds numbers; this type, however, did not exhibit a stagnation of the axial flow. Remarkably, a total of six different modes of vortex disruption were identified and cataloged in a comprehensive flow visualization study by Faler and Leibovich.⁵ More detail regarding vortex breakdown and stability can be found in two excellent surveys by Leibovich.^{6,7}

Since past theoretical attempts have considered the breakdown mechanism to be symmetric in nature, effects caused by asymmetries have been deemed incidental. For this reason, the loss of symmetry that accompanies three-dimensional vortex breakdown in tubes has been recently investigated by Beran and Culick.⁸ In their study, the non-unique solutions that were numerically reproduced at sufficiently large Reynolds numbers coincided with the sudden formation of reversed flow when the vortex circulation reached a critical value. At this juncture, it became impossible to numerically integrate the approximate form of the parabolized, quasi-cylindrical, Navier-Stokes equations. This result supported the theory advanced much earlier by Hall.⁹ Hall's methodology was analogous to the shallow-water wave theory or the plane flow separation theory according to which the position of the separation point could be signaled by the breakdown of the boundary-layer equations.

Due to the recirculatory patterns associated with vortex propagation and breakdown, the application of swirl has been extensively used as a vehicle for efficient and stable combustion in industrial furnaces, utility

boilers, spiral heat exchangers, gas turbines with toroidal zones, turbofans with swirl augmentors, internal combustion engines, and other vortex burners (see Lilley¹⁰). In these applications, swirl is imparted to the primary and/or secondary jets to enhance their size, entrainment, and/or decay. Due to the swelling that accompanies vortex breakdown, swirling jets are also used as flame-holders with controllable flame characteristics affecting their shape, stability, and combustion intensity.

In swirl combustors a distinction can be made between tangentially fired and wall-fired equipment. Sometimes the oxidizer is introduced through an annulus surrounding a central jet of fuel. If the fuel enters as liquid droplets or solid particles, it is either atomized or sprayed from the core region. Typically, either coswirl or counterswirl configurations are induced in the inner and outer jets to promote intense and stable flames. Whereas coswirl leads to better combustion efficiencies, counterswirl generates a relatively larger recirculatory zone, a shorter luminous combustion zone, and a larger slip velocity and turbulent intensity along the interjet layer. The coswirling arrangement produces a slightly shorter flame and a weaker sensitivity to changes in hardware and operating conditions (see Gupta, Lilley and Syred,¹¹ and Durbin and Ballal¹²).

The degree of swirl is often quantified by the dimensionless swirl number S which scales with the ratio of tangential swirl to axial momentum forces. For strong swirl ($S > 0.6$) breakdown manifestation begins to develop beyond a critical Reynolds number that marks the transition from the supercritical to the subcritical flow regimes. In the wake of the recirculatory bubble formation that accompanies breakdown, a spiraling vortex disturbance is often detected. This disturbance is generally unsteady in position, exhibiting axial excursions in an unpredictable way. This so-called precessing vortex enhances mixing, combustion intensity, and flame length. However, it leads to combustion oscillations, noise, and pollutant formation. Active control strategies could then be called upon to suppress thermoacoustic instabilities by using, for example, acoustic excitation with phase-shifting. This approach can be implemented to decouple the pressure and heat release fluctuations as shown by Paschereit, Gutmark, and Weisenstein.¹³ In the wake of rotors in aeroengines, the pairing of acoustico-vortical disturbances in a slowly varying cylindrical duct is another topic that has been recently brought up by Cooper and Peake.¹⁴ In the interim, mean flow modeling of vortex burners has continued to receive attention through the work of Borissov, Shtern, and Hussain.¹⁵

As noted by Reydon and Gauvin,¹⁶ other technological processes in which swirl motion is critical to their proper operation include spray dryers, spray coolers, gas scrubbers, oil-water separators, cyclonic dust separators, hydraulic cyclones, and gas core nuclear rockets with magneto-hydrodynamic swirl (Love and Park¹⁷).

In practice, gas and hydro cyclones are used extensively in the petrochemical, mineral, and powder processing industries. Chiefly, they are employed in catalyst or product recovery, scrubbing, and dedusting. A cyclone separator typically consists of an upper cylindrical can with a central outlet tube and a lower conical section with bottom opening (see Fig. 1). An involute inlet tube at the head end permits the tangential injection of liquid or gaseous mixtures. Due to centrifugal accelerations and drag, denser and coarser particles are forced to the conical walls. The heavier particles are then swept downward to the base (or spigot) where the underflow is let out.

In view of the spatial decrease in cross-sectional area in the conical portion of the tube, the downward spiraling flow is compelled to reverse direction and exit through the top. The top opening is known as the vortex finder and consists of a tubular nozzle through which the overflow is discharged. The overflow carries the finer and lighter particles whose statistical size prescribes the efficiency of the cyclone. High efficiency cyclones are those capable of recovering 50% of the outflow particles with 2 microns or less in diameter.

Unlike columnar flows, cyclonic flows are characterized by a bidirectional coaxial motion that is not caused by vortex breakdown or instability. Due to the flow reversal in the conical section, the primary flow is forced to turn around as the core is approached. The ensuing bipolar motion is characterized by the presence of a non-translating layer separating the upward and downward drafts. This spinning layer is often referred to as the mantle.

One of the earliest investigations of cyclonic motions was carried out by ter Linden¹⁸ whose efforts have focused on determining the influence of geometric parameters on the separation efficiency in dust separators. His experimental work was quickly followed by the well known treatment of hydraulic and gas cyclones by Kelsall¹⁹ and Smith,^{20,21} respectively. These experiments were the first to suggest the existence of a forced vortex near the axis of the cyclone. Prior to these studies, it was widely assumed that a free vortex rather prevailed over the entire chamber volume.

Theoretical analysis of the conical hydro cyclone was initiated using semi-empirical approaches by Fontein and Dijkstra.²² It was followed by the

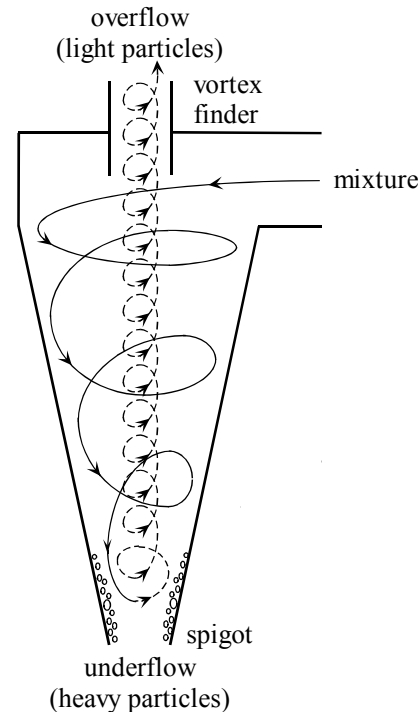


Fig. 1 Sketch of a conical cyclone separator.

momentum-integral analysis of cylindrical gas cyclones with flat base by Smith.^{20,21} These models were later refined by Bloor and Ingham²³ who employed the Polhausen method to account for inlet flow conditions. In spite of being based on a qualitative knowledge of the flow, the approximate solution by Bloor and Ingham²³ showed good agreement with experimental measurements obtained by Kelsall.¹⁹ Using laboratory tests as benchmarks, simple mathematical models were later furnished by Reydon and Gauvin,¹⁶ Vatisas, Lin and Kwok,^{24,25} Vatisas,²⁶ and others.

In subsequent years, a simple analytical model for the flow in a conical cyclone evolved from the work of Bloor and Ingham.²⁷ Unlike earlier studies that had precluded direct input of inlet conditions, theirs was inviscid and utilized realistic boundary conditions. In paving the way for an analytical solution, Bloor and Ingham²⁷ assumed that the mean flow vorticity was everywhere inversely proportional to the distance from chamber axis. This assumption enabled the extraction of a closed-form approximation for the bulk fluid motion. In fact, Bloor and Ingham's approximation proved quite useful in reproducing the overall features of the cyclonic flow. Numerical simulations were later carried out by Hsieh and Rajamani,²⁸ Hoekstra, Derksen and Van den Akker,²⁹ Derksen and Van den Akker,³⁰ and others. Hoekstra and co-workers also conducted laboratory tests using laser-doppler velocimetry (LDV) to verify their multi-phase numerical simulations.

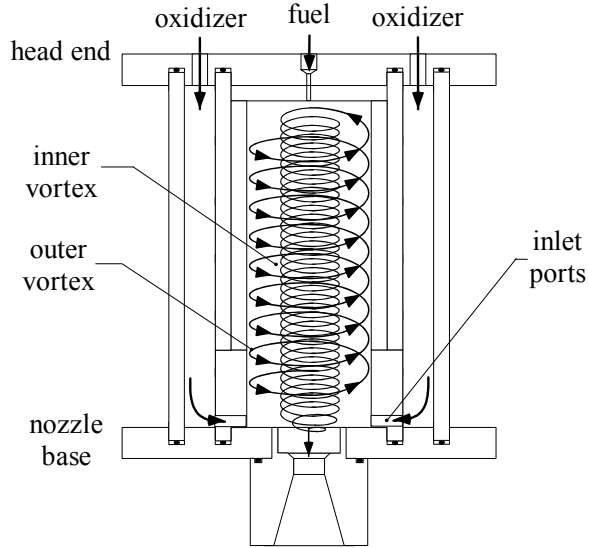


Fig. 2 Sketch of a bidirectional swirl chamber.

II. Current Technological Interest

While the general interest in improving industrial cyclones continues, the implementation of a fully reversing bidirectional swirl has been recently prompted by an original propulsion application. This application concerns the development of a lightweight combustion chamber that exhibits several technological advantages. The new prototype has been recently proposed by Chiaverini *et al.*³¹ and consists of an unconventional thrust chamber. Here the oxidizer is injected just upstream of the nozzle entrance and tangentially to the inner walls (see Fig. 2). After entering the chamber at the base, the oxidizer spirals toward the head end where fuel is added. Being prevented from crossing the closed end, the entrained oxidizer-fuel mixture then reverses and spirals inwardly toward the nozzle. The reversed flow is characterized by higher swirl velocities.

As in cyclones, a non-translating mantle separates the outer updraft from the inner downdraft, thus confining combustion products to the inner vortex tube. The inner swirl increases fuel residence time, turbulence, and propellant mixing, thus improving overall efficiency and thrust. It also allows for shorter chamber lengths. The outer vortex protects the chamber walls from excessive heating loads, thus resulting in lower wall temperatures. This feature not only reduces cooling requirements, but also permits more flexibility in material selection that ensures durability and reduced weight.

Unlike cyclonic flows that possess dual outlets, the bidirectional coaxial field observed in the liquid propellant thrust chamber has only one outlet section. In

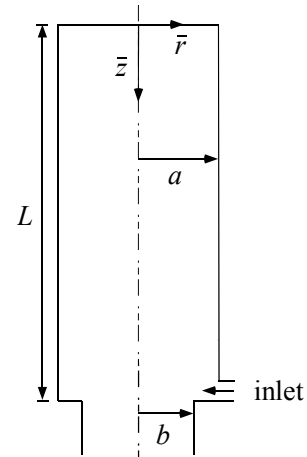


Fig. 3 Idealized chamber and coordinate system.

order to better understand its formation and stability to spatial and periodic disturbances, it would be of great benefit if particularly simple forms for the velocity and pressure components could be obtained. For this reason, it is the purpose of this study to provide, in a series of related articles, closed-form approximations that can be used to describe the bulk gas motion in this particular swirl-driven liquid propellant thrust chamber.

The current article summarizes our first attempt to provide an exact analytical solution to this problem with the aim of confirming its physicality. To that end, the Euler equations will be used as a starting point.

III. Mathematical Model

Our idealized chamber is modeled as a cylindrical tube of length L having a closed head end and a partially open downstream end that is attached to a tubular nozzle of radius b . A sketch of the chamber is given in Fig. 3 where \bar{r} and \bar{z} are used to designate the radial and axial coordinates. The present study is focused on describing the flowfield in the portion of the chamber extending from the head end to the base. Downstream of the base, the flow may accelerate by expanding through the nozzle. The fraction of the radius that is open to flow at the base is given by $\beta = b/a$ and the chamber's aspect ratio is given by $l = L/a$.

At the base, an aperture in the sidewall permits the tangential injection of an incompressible fluid (in the azimuthal or swirl direction). The assumption of incompressibility is not a restrictive one as the bidirectional vortex has been observed in the flows of both liquids and gases at low speed. The effects of compressibility may become important in the nozzle and are beyond the scope of this study. The forthcoming development is hence applicable to the bidirectional flow of either a liquid or a gas in the cylindrical portion of the tube ($0 \leq z \leq l$).

Since the purpose of the aperture is to permit the tangential injection of the fluid, the axial extent of this aperture is assumed to be small by comparison with the length of the chamber. Without loss in generality, the distribution of this thin aperture along the tube's circumference at the base may be taken to be uniform, thus mimicking a line source. For an inviscid fluid, the aperture could consist of one or several ports so long as it permits the injection of a rotationally symmetric flow. It must be borne in mind, however, that the actual three-dimensional flow into the chamber will become nearly axisymmetric only after the fluid has traveled some finite distance inside the chamber. In the present model, we ignore this small distance near the base which is practically needed for axisymmetric flow development.

A. Equations

After entering the chamber, fluid particles follow a helical trajectory traversing the entire length of the chamber twice before exiting at the base. Since our goal is to quantify the bulk gas motion under moderate to large mean flow Reynolds numbers, the small amount of fuel that is administered at the head end will be ignored in the global flow assessment. The present study will focus on the cold-flow motion that ensues under non-reactive or weakly reactive conditions. In summary, our flow will be (i) steady, (ii) inviscid, (iii) incompressible, (iv) rotational, and (v) non-reactive. Pursuant to these assumptions, the equations of motion can be written in standard vector and scalar notations. As usual, continuity is expressed by

$$\bar{\nabla} \cdot \bar{\mathbf{u}} = 0 \quad (1)$$

$$\frac{1}{\bar{r}} \frac{\partial(\bar{r}\bar{u}_r)}{\partial\bar{r}} + \frac{1}{\bar{r}} \frac{\partial\bar{u}_\theta}{\partial\theta} + \frac{\partial\bar{u}_z}{\partial\bar{z}} = 0 \quad (2)$$

while Euler's equations can be expanded as

$$\rho(\bar{\mathbf{u}} \cdot \bar{\nabla}\bar{\mathbf{u}}) = -\bar{\nabla}\bar{p} \quad (3)$$

$$\bar{u}_r \frac{\partial\bar{u}_r}{\partial\bar{r}} + \frac{\bar{u}_\theta}{\bar{r}} \frac{\partial\bar{u}_r}{\partial\theta} + \bar{u}_z \frac{\partial\bar{u}_r}{\partial\bar{z}} - \frac{\bar{u}_\theta^2}{\bar{r}} = -\frac{1}{\rho} \frac{\partial\bar{p}}{\partial\bar{r}} \quad (4)$$

$$\bar{u}_r \frac{\partial\bar{u}_\theta}{\partial\bar{r}} + \frac{\bar{u}_\theta}{\bar{r}} \frac{\partial\bar{u}_\theta}{\partial\theta} + \bar{u}_z \frac{\partial\bar{u}_\theta}{\partial\bar{z}} + \frac{\bar{u}_\theta\bar{u}_r}{\bar{r}} = -\frac{1}{\rho\bar{r}} \frac{\partial\bar{p}}{\partial\theta} \quad (5)$$

$$\bar{u}_r \frac{\partial\bar{u}_z}{\partial\bar{r}} + \frac{\bar{u}_\theta}{\bar{r}} \frac{\partial\bar{u}_z}{\partial\theta} + \bar{u}_z \frac{\partial\bar{u}_z}{\partial\bar{z}} = -\frac{1}{\rho} \frac{\partial\bar{p}}{\partial\bar{z}} \quad (6)$$

In conformance with previous studies of vortex flows, two further assumptions are made (see Leibovich⁷). The first is that of axisymmetry, which is well justified in a frictionless environment. The second is actually a byproduct of axisymmetry and frictionless motion. It involves specifying a swirl velocity that is independent of the axial coordinate. In the absence of

friction at the wall and between fluid layers, the angular momentum is clearly conserved in the axial direction. At the outset, the sensitivity of the swirl velocity to axial variations becomes immaterial. This result has been routinely adopted in the literature and is well explained in the work of Leibovich,^{6,7} Beran and Culick,⁸ Bloor and Ingham,^{23,27} Vatisas, Lin and Kwok,^{24,25} Szeri and Holmes,³² and others. Based on these idealizations, the equations of motion become

$$\frac{1}{\bar{r}} \frac{\partial(\bar{r}\bar{u}_r)}{\partial\bar{r}} + \frac{\partial\bar{u}_z}{\partial\bar{z}} = 0 \quad (7)$$

$$\bar{u}_r \frac{\partial\bar{u}_r}{\partial\bar{r}} + \bar{u}_z \frac{\partial\bar{u}_r}{\partial\bar{z}} - \frac{\bar{u}_\theta^2}{\bar{r}} = -\frac{1}{\rho} \frac{\partial\bar{p}}{\partial\bar{r}} \quad (8)$$

$$\bar{u}_r \frac{\partial\bar{u}_\theta}{\partial\bar{r}} + \frac{\bar{u}_\theta\bar{u}_r}{\bar{r}} = 0 \quad (9)$$

$$\bar{u}_r \frac{\partial\bar{u}_z}{\partial\bar{r}} + \bar{u}_z \frac{\partial\bar{u}_z}{\partial\bar{z}} = -\frac{1}{\rho} \frac{\partial\bar{p}}{\partial\bar{z}} \quad (10)$$

B. Boundary Conditions

The first set of boundary conditions are due to symmetry and the infinite impedance of the walls. The second set is due to the inlet configuration and bulk mass conservation. Physically, these consist of

- a fully tangential inflow,
- a zero axial flow at the head end,
- symmetry about the centerline,
- a zero radial flow at the walls, and
- an inflow that matches the outflow at the base.

These particular conditions translate into

$$\begin{cases} \bar{r} = a, \bar{z} = L, \bar{u}_\theta = U \\ \bar{z} = 0, \forall \bar{r}, \bar{u}_z = 0 \\ \bar{r} = 0, \forall \bar{z}, \bar{u}_r = 0 \\ \bar{r} = a, \forall \bar{z}, \bar{u}_r = 0 \\ \bar{z} = L, \bar{Q}_i = \bar{Q}_o = UA_i \end{cases} \quad (11)$$

where \bar{Q}_i and \bar{Q}_o represent the volumetric flow rates at the chamber inlet and outlet, respectively.

C. Normalization

In seeking a similarity solution to the problem, it is helpful to normalize all variables. Our choice relies on

$$z = \frac{\bar{z}}{a}; \quad r = \frac{\bar{r}}{a}; \quad \nabla = a\bar{\nabla}; \quad \beta = \frac{b}{a} \quad (12)$$

$$u_r = \frac{\bar{u}_r}{U}; \quad u_\theta = \frac{\bar{u}_\theta}{U}; \quad u_z = \frac{\bar{u}_z}{U} \quad (13)$$

$$p = \frac{\bar{p}}{\rho U^2}; \quad Q_i = \frac{\bar{Q}_i}{Ua^2} = \frac{A_i}{a^2}; \quad Q_o = \frac{\bar{Q}_o}{Ua^2} \quad (14)$$

Here $U = \bar{u}_\theta(a, L)$ represents the average fluid injection velocity and b refers to the radius of the nozzle. It should be noted that the proper normalization of \bar{Q}_i is not arbitrary, but rather dictated by

$$\frac{\bar{Q}}{Q} = \frac{\int \bar{\mathbf{u}} \cdot \hat{\mathbf{n}} \bar{r} d\bar{r} d\theta}{\int \mathbf{u} \cdot \hat{\mathbf{n}} r dr d\theta} = Ua^2 \quad (15)$$

Clearly, it is fixed by our current choice for \mathbf{u} and r .

Another important realization is the relation between the normalized volumetric flow rate \bar{Q}_i and the swirl number S used in the literature. According to Hoekstra, Derksen and Van den Akker,²⁹ the swirl number appropriate of cyclonic flows may be written as

$$S \equiv \frac{\pi ab}{A_i} = \frac{\pi \beta a^2}{A_i} = \frac{\pi \beta}{Q_i} = \pi \beta \sigma \quad (16)$$

where the reciprocal of the normalized volumetric flow rate represents a modified swirl number, $\sigma \equiv Q_i^{-1}$. As expected, the swirl number is increased when the inlet area is reduced at fixed volumetric flow rate.

Pursuant to Eqs. (12)–(14), the dimensionless conservation equations become

$$\nabla \cdot \mathbf{u} = 0; \quad \mathbf{u} \cdot \nabla \mathbf{u} = -\nabla p \quad (17)$$

After substituting $\mathbf{u} \cdot \nabla \mathbf{u} = \frac{1}{2} \nabla(\mathbf{u} \cdot \mathbf{u}) - \mathbf{u} \times \nabla \times \mathbf{u}$ into Eq. (17), one can eliminate the pressure, as usual, by taking the curl of the momentum equation. This operation yields

$$\nabla \times \mathbf{u} \times \boldsymbol{\Omega} = 0; \quad \boldsymbol{\Omega} \equiv \nabla \times \mathbf{u} \quad (18)$$

where mean flow vorticity is given by $\boldsymbol{\Omega} \equiv \nabla \times \mathbf{u}$. The normalized boundary conditions reduce to

$$\begin{cases} u_\theta(1, l) = 1; & u_z(r, 0) = 0; & u_r(0, z) = 0 \\ u_r(1, z) = 0; & Q_0 = \int_0^{2\pi} \int_0^\beta \mathbf{u}(r, l) \cdot \hat{\mathbf{n}} r dr d\theta = Q_i \end{cases} \quad (19)$$

where $\mathbf{u} \cdot \hat{\mathbf{n}} = u_z$ represents the outflow velocity at the base.

IV. Solution

Having specified the particular conditions that bring closure to our model, a solution for Eq. (18) can be attempted.

A. A Free Vortex

Before proceeding further, it may be helpful to consider the θ -momentum equation. Based on the normalized form of Eq. (9), it can be seen that

$$u_r \left(\frac{\partial u_\theta}{\partial r} + \frac{u_\theta}{r} \right) = 0 \quad (20)$$

One deduces that, regardless of u_r , the azimuthal component must be of the form

$$u_\theta = A/r \quad (21)$$

Equation (21) confirms the presence of a free vortex type distribution that is independent of the axial location. The establishment of free vortex motion can be directly attributed to angular momentum conservation of a frictionless fluid. The first boundary condition in Eq. (19), namely $u_\theta(1, l) = 1$, ensures that the flow enters the chamber tangentially to the inner circumference. One finds $A = 1$ or

$$u_\theta = 1/r \quad (22)$$

This result has an immediate consequence on vorticity. Based on Eq. (21), both radial and axial components of vorticity are eliminated. One is left with

$$\Omega_r = 0; \quad \Omega_\theta = \frac{\partial u_r}{\partial z} - \frac{\partial u_z}{\partial r}; \quad \Omega_z = 0 \quad (23)$$

The cancellation of radial and axial vorticity components simplifies the vorticity transport equation given by Eq. (18).

B. Decoupled Equations

At this juncture, both radial and axial velocity components remain to be determined from the reduced set given by

$$\frac{1}{r} \frac{\partial(ru_r)}{\partial r} + \frac{\partial u_z}{\partial z} = 0 \quad (\text{continuity}) \quad (24)$$

$$\frac{\partial(u_r \Omega_\theta)}{\partial r} + \frac{\partial(u_z \Omega_\theta)}{\partial z} = 0 \quad (\text{vorticity transport}) \quad (25)$$

$$\frac{\partial u_r}{\partial z} - \frac{\partial u_z}{\partial r} = \Omega_\theta \quad (\text{vorticity}) \quad (26)$$

Realizing that the swirl velocity is decoupled from the remaining set, the introduction of the Stokes stream function appears to be a possibility despite the overall three-dimensionality of the velocity field. As usual, the Stokes stream function ψ in cylindrical coordinates can be expressed by

$$u_r = -\frac{1}{r} \frac{\partial \psi}{\partial z}; \quad u_z = \frac{1}{r} \frac{\partial \psi}{\partial r} \quad (27)$$

When this transformation is used in the vorticity transport equation given by Eq. (25), one obtains

$$-\frac{\partial \psi}{\partial z} \frac{\partial}{\partial r} \left(\frac{\Omega_\theta}{r} \right) + \frac{\partial \psi}{\partial r} \frac{\partial}{\partial z} \left(\frac{\Omega_\theta}{r} \right) = 0 \quad (28)$$

and so

$$\left(\frac{\Omega_\theta}{r} \right)_z = \frac{\psi_z}{\left(\frac{\Omega_\theta}{r} \right)_r} = \frac{\psi_r}{\left(\frac{\Omega_\theta}{r} \right)_r} \quad (29)$$

The resulting equality will hold if, and only if,

$$\Omega_\theta = rF[\psi(r, z)] \quad (30)$$

When this classic form is substituted into Eq. (29), it can be promptly seen that

$$\frac{(\Omega_\theta / r)_z}{(\Omega_\theta / r)_r} = \frac{[F(\psi)]_z}{[F(\psi)]_r} = \frac{F_\psi \psi_z}{F_\psi \psi_r} = \frac{\psi_z}{\psi_r} \quad (31)$$

C. Vorticity-Stream Function Approach

According to Eq. (30), F can be a general function of ψ . One of the simplest cases corresponds to a linear relationship of the form $F = C^2 \psi$; hence, one can put

$$\Omega_\theta = C^2 r \psi \quad (32)$$

This linear choice is guided by the desire to seek an exact solution for this problem. It is also inspired by the success of a similar relation that was formerly used to obtain the bulk gas description inside a simulated solid rocket motor (see Culick³³). Bearing in mind that other possible solutions may exist, we now proceed and substitute Eq. (32) into the remaining vorticity equation given by Eq. (26). At the outset, a linear partial differential equation is produced for ψ ; this is

$$\frac{\partial^2 \psi}{\partial z^2} + \frac{\partial^2 \psi}{\partial r^2} - \frac{1}{r} \frac{\partial \psi}{\partial r} + C^2 r^2 \psi = 0 \quad (33)$$

In turn, three of the boundary conditions may be conveniently written for the stream function. Based on Eq. (19), one gathers

$$\begin{cases} z = 0; & u_z = 0; & \partial \psi / \partial r = 0 \\ r = 0; & u_r = 0; & \partial \psi / \partial z = 0 \\ r = 1; & u_r = 0; & \partial \psi / \partial z = 0 \end{cases} \quad (34)$$

D. General Solution

Clearly, Eq. (33) is separable. One can proceed by setting

$$\psi(r, z) = f(r)g(z) \quad (35)$$

This decomposes Eq. (33) into

$$-\frac{1}{g} \frac{d^2 g}{dz^2} = \frac{1}{f} \left(\frac{d^2 f}{dr^2} - \frac{1}{r} \frac{df}{dr} + C^2 r^2 f \right) = \pm \lambda^2 \quad (36)$$

where λ is a separation constant.

For a nonzero λ , the stream function exhibits either trigonometric or hyperbolic variations in the axial direction. Based on the present knowledge base, such physical behavior is unlikely to occur. The possibility of a nonzero separation constant is hence ruled out. The only plausible choice is attendant on $\lambda = 0$. On the one hand, this value leads to a linear axial variation of the form $g(z) = C_1 z + C_2$. On the other, it permits extracting the radial variation of the stream function from the Bessel equation

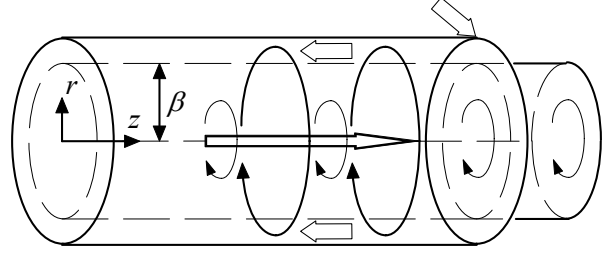


Fig. 4 Chamber outline and mantle location.

$$\frac{d^2 f}{dr^2} - \frac{1}{r} \frac{df}{dr} + C^2 r^2 f = 0 \quad (37)$$

such that

$$f(r) = r D_3 J_{1/2} \left(\frac{1}{2} C r^2 \right) + r D_4 J_{-1/2} \left(\frac{1}{2} C r^2 \right) \quad (38)$$

Then using the known identities,

$$J_{1/2}(x) = \sqrt{2/(\pi x)} \sin(x); \quad J_{-1/2}(x) = \sqrt{2/(\pi x)} \cos(x) \quad (39)$$

one can put

$$f(r) = C_3 \sin \left(\frac{1}{2} C r^2 \right) + C_4 \cos \left(\frac{1}{2} C r^2 \right) \quad (40)$$

The general form of the stream function becomes

$$\psi = (C_1 z + C_2) \left[C_3 \sin \left(\frac{1}{2} C r^2 \right) + C_4 \cos \left(\frac{1}{2} C r^2 \right) \right] \quad (41)$$

E. Particular Solution

Using the constraints associated with Eq. (34) one can evaluate the general constants. Firstly, due to the vanishing axial velocity at the head end, it can be inferred that $C_2 = 0$. This leaves

$$\psi = C_1 z \left[C_3 \sin \left(\frac{1}{2} C r^2 \right) + C_4 \cos \left(\frac{1}{2} C r^2 \right) \right] \quad (42)$$

Secondly, axisymmetry via $u_r(0, z) = 0$ implies that $C_4 = 0$. Thirdly, as u_r vanishes along the hard walls, one must have

$$C_1 C_3 \sin \left(\frac{1}{2} C \right) = 0 \quad (43)$$

Realizing that neither $C_1 = 0$ nor $C_3 = 0$ are acceptable outcomes, one is left with $\sin \left(\frac{1}{2} C \right) = 0$; forthwith, a fundamental solution can be associated with $C = 2\pi$. Consequently, one can put

$$\psi = B z \sin(\pi r^2); \quad B \equiv C_1 C_3 \quad (44)$$

At length, the velocity field reduces to

$$\mathbf{u} = -\frac{B}{r} \sin(\pi r^2) \mathbf{e}_r + \frac{1}{r} \mathbf{e}_\theta + 2B\pi z \cos(\pi r^2) \mathbf{e}_z \quad (45)$$

The last constant can be determined from a global mass balance. Based on the sketch in Fig. 4, mass flowing into the chamber must be discharged at the base

through the port of dimensionless radius β . As $Q_0 = Q_i$, one must have

$$2\pi \int_0^\beta \mathbf{u} \cdot \hat{\mathbf{n}} \, r \, dr = 2\pi \int_0^\beta u_z \, r \, dr = Q_i \quad (46)$$

hence,

$$B = Q_i \csc(\pi\beta^2) / (2\pi l) \quad (47)$$

and so

$$\begin{aligned} \mathbf{u} &= -\frac{Q_i \sin(\pi r^2)}{2\pi l \sin(\pi\beta^2) r} \mathbf{e}_r + \frac{1}{r} \mathbf{e}_\theta + \frac{Q_i z}{l \sin(\pi\beta^2)} \cos(\pi r^2) \mathbf{e}_z \\ &= -\frac{\sin(\pi r^2)}{2\pi \sigma l \sin(\pi\beta^2) r} \mathbf{e}_r + \frac{1}{r} \mathbf{e}_\theta + \frac{z \cos(\pi r^2)}{\sigma l \sin(\pi\beta^2)} \mathbf{e}_z \end{aligned} \quad (48)$$

Having formulated the velocity field, the pressure gradients in the radial and axial directions can be deduced. From Eq. (17), one finds

$$\frac{\partial p}{\partial r} = \frac{4\sigma^2 l^2 \pi^2 \sin^2(\pi\beta^2) + \sin^2(\pi r^2) - \pi r^2 \sin(2\pi r^2)}{4\sigma^2 l^2 \pi^2 r^3 \sin^2(\pi\beta^2)} \quad (49)$$

and

$$\frac{\partial p}{\partial z} = -\frac{z \csc^2(\pi\beta^2)}{\sigma^2 l^2} \quad (50)$$

Based on the partial integration of these pressure gradients, the spatial distribution of the pressure may be fully determined. This analysis will be later carried out after prescribing the key geometric ratio β .

V. Discussion

Having obtained the general form of the bi-directional vortex, its distinct flow attributes can now be examined. In our problem, the characteristic features of the velocity and pressure profiles can be quantified along the chamber length and cross section by varying the chamber aspect ratio in addition to the inlet and outlet area ratios.

A. Analytical and Computational Predictions

Before describing the flowfield based on the current formulation, it may be instructive to present a sample of the numerical results obtained recently by an independent group of investigators who employed a commercial package dubbed FDNS. This computational fluid dynamics (CFD) code specializes in solving the coupled, three-dimensional Navier-Stokes equations for a chemically reactive, multi-phase and compressible flow. FDNS is a second-order accurate, finite volume code with an all-speed formulation ranging from low speeds to hypersonic regimes. Specifically, it utilizes multi-block mesh systems to model complex geometry.

FDNS was run using finite-rate chemistry, three-dimensional analysis, and an adiabatic wall specification for calculating chamber wall heat fluxes.

In our problem, a finite-rate oxygen-hydrogen combustion chemistry was used in the simulation of the liquid thrust chamber. The nominal mesh consisted of 184×35 axial and radial grid cells. This included 12 grid cells in the axial direction to resolve the injection area. The grid cell spacing in both the radial and axial directions was non-uniform to permit better grid concentration near the walls and near regions of higher flow gradients.

Using an aspect ratio of $l = 3.42$, $A_i = 10^{-3} \text{ m}^2$, $U = 260 \text{ m s}^{-1}$, $\rho = 2.24 \text{ kg m}^{-3}$, $\dot{Q}_i = 0.26 \text{ m}^3 \text{ s}^{-1}$, $\mu = 9.6 \times 10^{-5} \text{ kg m}^{-1} \text{ s}^{-1}$, $a = 0.0673 \text{ m}$, and a Reynolds number of $Re = 4 \times 10^5$, the vector field obtained by the CFD solver is shown in Fig. 5a. Using a similar geometry and flow intensity, the vector plot produced from Eq. (48) is displayed in Fig. 5b for a nozzle outlet ratio corresponding to $\beta = 0.707$.

Despite the disparity in the governing equations and assumptions used in the present work vis-à-vis those employed in the CFD simulations, it is interesting to note the favorable agreement between theory and computation. In both cases, the flow enters at the base, travels upwardly, and then turns sharply near the head end; after reversing direction at the chamber head end, the flow returns to the base area where it exits through the open nozzle section. Based on the CFD solution, the thin boundary layer near the chamber wall is too small to be discerned graphically. The small size of this layer lends support to the inviscid assumption used in our study; this idealization seems to hold well near the wall.

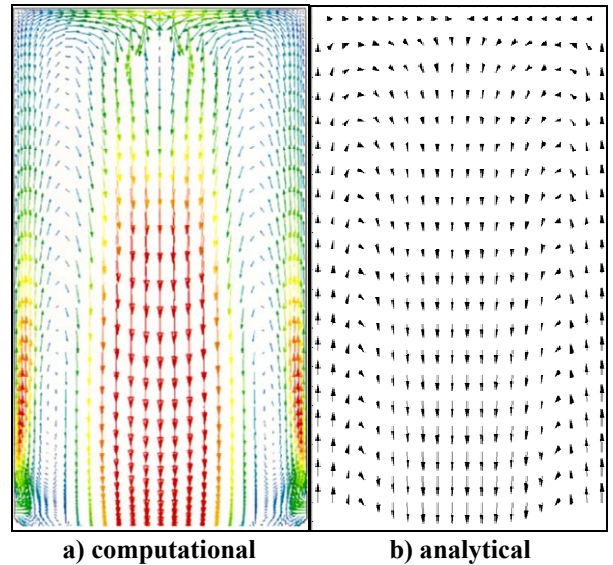


Fig. 5 Vector plots comparing CFD results with the current analytical predictions.

Along the corners of the head end and base sections, the gradual flow curvature that is captured by the Navier-Stokes solver is due to viscous effects that elude the analytical model. Nonetheless, both analytical and numerical solutions confirm the existence of cross flow between the outer and inner vortex regions along the length of the chamber. They also confirm the presence of the so-called mantle separating the outer and inner vortex tubes. Since the upward spinning outer vortex consists of the annular flow with negative axial velocity, it occupies the region delineated by $\beta^* < r < 1$; here β^* designates the radius of the mantle where the axial velocity switches signs. In the same context, the inner vortex remains confined to the cylindrical region with positive axial velocity, $0 < r < \beta^*$.

B. Theoretical Location of the Mantle

Clearly, the mantle represents a non-translating yet rotating layer that serves to demarcate the axial flow directed toward the head end from that directed toward the nozzle. This layer forms the envelope along which the axial component of the velocity vanishes. It can be determined from the root $r = \beta^*$ for which $u_z = 0$ in Eq. (48). This value can be obtained from

$$Q_i(z/l) \csc(\pi\beta^2) \cos(\pi\beta^{*2}) = 0 \quad (51)$$

thus yielding

$$\beta^* = 1/\sqrt{2} \cong 0.70711 \quad (52)$$

It should be noted that $\beta^* = 1/\sqrt{2}$ is not the only root for Eq. (51). The possible existence of multiple roots and their corresponding geometric interpretations will be addressed in a separate study.

As illustrated in Fig. 5a, the presence of a non-translating layer at approximately 70.7% of the chamber radius appears to be in excellent agreement with recent CFD results. The latter exhibit a vanishing axial velocity at $r \cong 0.71$. In fact, our theoretical estimate appears to be in excellent agreement with the average value of 0.72 obtained experimentally by Smith²¹ in his cylindrical gas cyclone with flat base. Our estimate is also in good agreement with the average value of $\beta^* \cong 0.675$ predicted by the numerical and experimental studies of Hoekstra, Derksen and Van Den Akker.²⁹ These tests were carried out at a moderate Reynolds number of $Re = 5 \times 10^4$ and three decreasing swirl numbers of $S = 3.1$, 2.2 and 1.8 (cf. Fig. 5b, 5d, and 5f, p. 2061).²⁹ The small deviations from our predicted value of 0.707 may be attributed to the particular use of the Reynolds stress transport model (RSTM) and to geometric differences that are specific to gas cyclones.

In the gas cyclone, for example, the protrusion of a tubular outlet pipe known as the vortex finder aids in guiding the updrift in the vicinity of the head end where the overflow is discharged. Clearly, the protruding vortex finder can influence the equilibrium position of the mantle. In our model, the vortex finder is replaced by a tubular nozzle that does not protrude into the chamber. In contrast to the cyclonic setup, both inflow and outflow take place at the base of the chamber. In addition to the reversal in the role of gravity on the outgoing motion, the current model does not exhibit a secondary outlet (i.e., the cyclonic spigot) to collect the underflow. Despite these basic geometric differences, one should note that the agreement with reported measurements seems to improve at higher Re .²⁹

At first glance, the fixed position of the mantle may appear paradoxical, being independent of the inlet flow rate. Theoretically, the spatial determination of the mantle location may be ascribed to mass and momentum balances which, according to our similarity solution, will only be satisfied when the bidirectional flow is split at precisely $r = 1/\sqrt{2}$. So long as the similarity solution remains uninfluenced by inlet conditions except in its azimuthal component (see Eq. (48)), the radial lock on the mantle position is solely imposed by the necessary balances between axial and radial mass and momenta. This result has been confirmed experimentally by several reported measurements including those by Smith.²¹ An illustrative case is reproduced in Table 1 for a mean flow Reynolds number of 100,000 and several axial positions distributed along the chamber length. Within experimental uncertainty, the results obtained by Smith²¹ seem to support the theoretical mantle location.

In practice, it may be reassuring to note that the weak sensitivity of the mantle location to inlet flow conditions has been repeatedly confirmed by Vatisias, Lin and Kwok.^{24,25} Despite the basic geometric differences between their model and ours, it is gratifying to note the qualitative agreement with their analytical and experimental findings.

Table 1 Mantle location by Smith (1962)

Site	$L - \bar{z}$ [in]	\bar{r} [in]	Radial Fraction, β^*
1	0.0	2.13	0.7083
2	1.5	2.15	0.7166
3	3.0	2.15	0.7166
4	4.5	2.15	0.7166
5	6.0	2.17	0.7233
6	7.5	2.20	0.7333
7	9.0	2.20	0.7333
Mean		2.16	0.7211

C. Ideal Nozzle Opening

When the nozzle radius is smaller than the radius of the inner vortex ($\beta < \beta^*$), a collision will take place between the inner vortex and the wall at $z = l$. This collision triggers the development of a corner flow near the nozzle section. The downstream corner flow requires special treatment and cannot be captured by the current solution. Although corner flows are permitted in the entry section of a real nozzle, they are difficult to capture analytically. The suitability of our mathematical model may hence deteriorate as $\beta^* - \beta$ is increased with successive nozzle area contractions.

In converse manner, when the nozzle opening is allowed to extend beyond the mantle location (for $\beta > \beta^*$), the incoming stream that forms the outer vortex will not be restricted from escaping through the downstream opening. It will have the option to drift downwardly. This scenario may be unphysical as it stands to violate global mass conservation; the latter demands that the total incoming flux be directed toward the head end. The departure from physicality may hence be expected with successive increases in $\beta - \beta^*$.

The physical model depicted in Fig. 3 will be optimal when the diameter of the inner vortex matches the diameter of the nozzle at the base. This will prevent sudden flow obstructions and unwarranted secondary flows. By setting $\beta = \beta^*$ as in Fig. 4, the outflow will be aligned with the nozzle opening at the base, thus obviating the need for detailed assessment of fluid recirculation and corner vortices near $z = l$.

D. Velocity and Pressure Relations

By putting $\beta = \beta^* = 1/\sqrt{2}$, a complete expression for the velocity field can be obtained. In the interest of brevity, we define the geometric inflow parameter

$$\kappa \equiv \frac{Q_i}{2\pi l} = \frac{A_i}{2\pi aL} = \frac{1}{2} \frac{c^2}{a^2} \frac{a}{L} = \frac{1}{2\pi\sigma l} = \frac{1}{2\sqrt{2}Sl} \quad (53)$$

where $c = \sqrt{A_i}/\pi$ represents the effective inlet radius. In practical applications, κ is a small parameter. For ORBITEC's experiment, one may use $\sigma = 25.64$ and $l = 1$ to find $\kappa = 0.0137$.

By virtue of $\beta = 1/\sqrt{2}$, the modified swirl number takes the form

$$\sigma = \frac{\sqrt{2}}{\pi} S = \frac{1}{Q_i} = \frac{a^2}{A_i} \quad (54)$$

The complete bidirectional flow becomes expressible by

$$\psi = \kappa z \sin(\pi r^2) \quad (55)$$

$$\mathbf{u} = -\frac{\kappa}{r} \sin(\pi r^2) \mathbf{e}_r + \frac{1}{r} \mathbf{e}_\theta + 2\pi\kappa z \cos(\pi r^2) \mathbf{e}_z \quad (56)$$

Similarly, the pressure gradients reduce to

$$\frac{\partial p}{\partial r} = \frac{1 + \kappa^2 [\sin^2(\pi r^2) - \pi r^2 \sin(2\pi r^2)]}{r^3} \quad (57)$$

$$\frac{\partial p}{\partial z} = -4\pi^2 \kappa^2 z \quad (58)$$

To determine the pressure field from Eqs. (57)–(58) partial integration may be performed. At the outset, one finds

$$p = -\frac{2 + \kappa^2 - \kappa^2 \cos(2\pi r^2)}{4r^2} + c_1(z) \quad (59)$$

and

$$p = -2\pi^2 z^2 \kappa^2 + c_2(r) \quad (60)$$

By combining Eqs. (59) and (60), one can introduce $\Delta p = p - p_0$ where

$$\Delta p = -\frac{1}{2r^2} \left\{ 1 + \frac{1}{2} \kappa^2 [8\pi^2 r^2 z^2 + 1 - \cos(2\pi r^2)] \right\} \quad (61)$$

and p_0 is the pressure at the head-end center.

E. Confirmation of Bernoulli's Relation

Having obtained an inviscid rotational flow, one expects the sum of the pressure and kinetic energy to remain constant along a streamline. Using normalized quantities, Bernoulli's equation translates into

$$p + \frac{1}{2} \mathbf{u} \cdot \mathbf{u} = H(\psi) \quad (62)$$

Based on Eqs. (56) and (61), one finds, after some algebra, the expected result confirming that

$$H(\psi) = p_0 - 2\pi^2 \psi^2 = p + \frac{1}{2} \mathbf{u} \cdot \mathbf{u} \quad (63)$$

F. Cross Flow Velocity

It should be noted that a constant radial cross-flow velocity $(u_r)_{\text{cross}}$ exists at $r = 1/\sqrt{2}$. This radial influx is uniform along the mantle length and permits mass to be transported to the inner vortex, across the mantle surface. Due to the vanishing axial velocity and inability of the swirl component to transmit mass inwardly, $(u_r)_{\text{cross}}$ provides the only means of communication between the outer and inner vortex regions. Along the mantle length, the flow is constantly injected into the inner vortex at a rate equal to

$$(u_r)_{\text{cross}} = -\kappa\sqrt{2} = -\frac{1}{\sqrt{2}\pi\sigma l} \quad (64)$$

The negative sign merely indicates an inward flow direction. Interestingly, one may verify that the volumetric cross flow matches the inflow by integrating $(u_r)_{\text{cross}}$ over the mantle length; specifically, one finds

$$2\pi\beta \int_0^l |(u_r)_{\text{cross}}(\beta, z)| dz = Q_i \quad (65)$$

G. Flow Streamlines

To aid in flow visualization, the relations needed to trace the particle streamlines are determined from Eq. (44). Due to symmetry about the chamber axis, it is sufficient to describe the flow patterns in half of the domain. Under steady-state conditions, the streamlines are essentially particle pathlines. For simplicity, it is convenient to depict the streamlines in a two-dimensional $r-z$ plane. The particle path in a two dimensional plane can be extended to a three dimensional domain by superimposing the additional feature of swirl.

Several discrete streamlines are shown in Fig. 6 using three increasing chamber lengths corresponding to geometric aspect ratios of $L/a=1, 3$ and 5 . The avoidance of streamlines near the core and head-end regions is to reduce clutter near the wall. One can infer from Fig. 6 that a fluid particle entering the chamber travels along a helical trajectory, reverses direction at

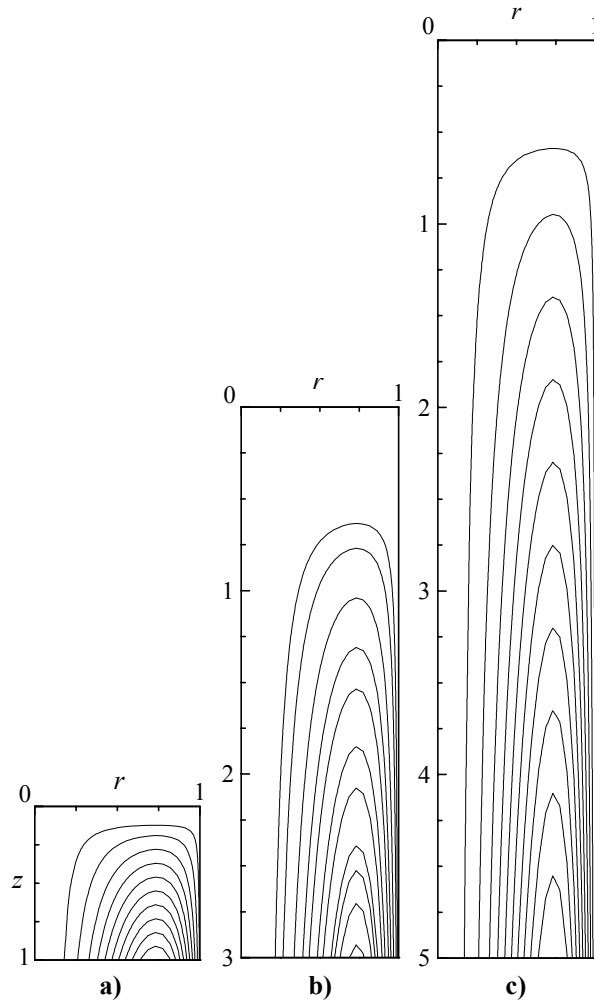


Fig. 6 Streamline patterns at three chamber aspect ratios of a) $L/a=1$, b) 3 , and c) 5 .

the head end, and then returns to the nozzle while spinning at a higher angular speed. The theoretical patterns appear to be in good agreement with either computational or experimental results obtained by Smith,^{20,21} Vastatas, Lin and Kwok,^{24,25} and Hoekstra, Derksen and Van Den Akker.²⁹

H. Axial Velocity Distribution

The axial velocity distribution, described by u_z in Eq. (56), is a linear function of the axial distance from the chamber head end. Accordingly, the axial velocity linearly decreases as the fluid approaches the head end; conversely, it is seen to accelerate in the downstream direction. This behavior is captured in Fig. 7a where the radial distribution of the axial velocity is shown at several axial stations. As one would expect, the maximum axial velocity is reached as the fluid exits along the chamber axis at $z=l$. This maximum velocity can be found to be $(u_z)_{\max} = Q_l$ via Eq. (56).

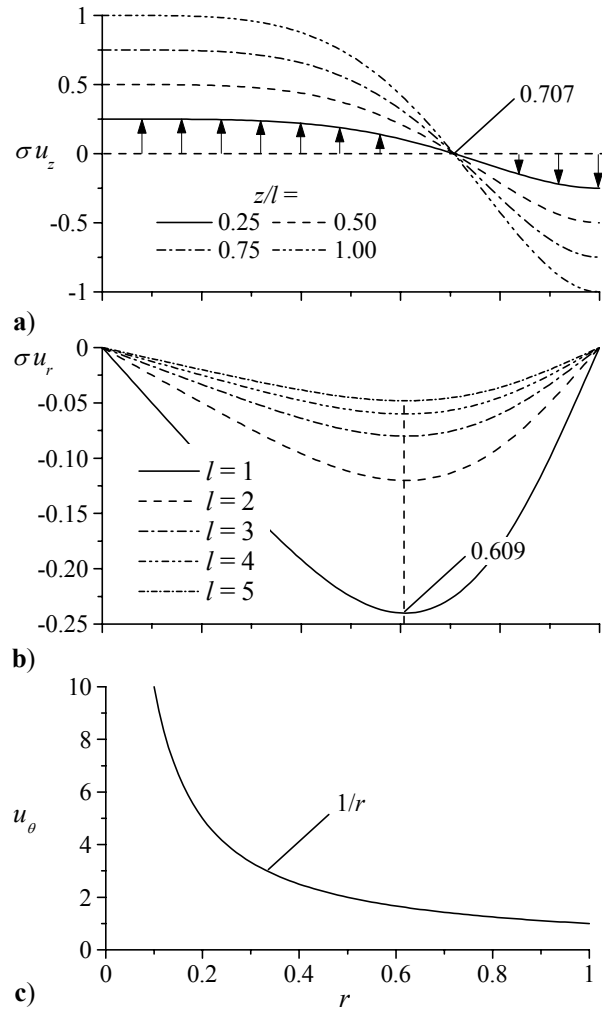


Fig. 7 Axial, radial, and azimuthal (swirl) velocity distributions along the chamber radius.

I. Radial Velocity Distribution

A plot of the radial velocity component is given in Fig. 7b for several chamber aspect ratios. Unlike solid or hybrid rocket motors, the radial velocity is zero along the sidewall as there is no gas injection normal to the wall. Interestingly, the radial velocity peaks in the vicinity of the mantle as shown in Fig. 7b. The location of the radial velocity maximum can be determined numerically or asymptotically. To calculate the location of the maximum radial velocity $(u_r)_{\max}$, one can set

$$\frac{du_r}{dr} = \left[-2\pi\kappa \cos(\pi r^2) + \frac{\kappa \sin(\pi r^2)}{r^2} \right]_{r_{\max}} = 0 \quad (66)$$

to find

$$\tan(\pi r_{\max}^2) - 2\pi r_{\max}^2 = 0 \quad (67)$$

Solving Eq. (67) numerically yields $r_{\max} \cong 0.609106$. This result compares favorably with the numerical estimate of 0.61 based on recent CFD results obtained by a team of researchers at ORBITEC.³⁴ Forthwith, the largest radial velocity magnitude associated with r_{\max} is found to be

$$(u_r)_{\max} \cong -1.50879\kappa = -0.24013/(\sigma l) \quad (68)$$

Equation (68) confirms the small size of u_r by comparison with u_z except near the head end where z and thereby u_z approach zero. It also suggests that a smaller radial velocity can be associated with more elongated chambers or higher swirl numbers.

Despite the accuracy of the inviscid solution in predicting fundamental flow characteristics, it is only adequate in mimicking the bulk features of the bidirectional fluid motion. Secondary details near the endwalls are not accounted for. Evidently, as u_r remains independent of z , the no-slip condition at the endwalls is relaxed. In the absence of friction between fluid layers and the wall, the radial velocity profile remains invariant at any axial location. In principle, enforcing slip at the endwalls can be later achieved using a viscous boundary layer treatment.

J. Azimuthal Velocity Distribution

Here too the azimuthal velocity depends on the radial coordinate only. Based on Eq. (56), the hyperbolic relation between velocity and radial distance from the chamber axis is illustrated in Fig. 7c.

Consistently with the radial velocity behavior, u_θ does not satisfy the no-slip boundary condition at the endwalls. Consistently with u_z , u_θ does not vanish along the sidewall either. The relaxation of the no-slip condition along the hard walls is consistent with the ideal fluid assumption made earlier. Allowing slip along the walls does not pose a serious restriction due to the small size of the attendant boundary layers. In

fact, the marginal importance of the viscous layer along the sidewall has been confirmed in past laboratory and numerical experiments. One may cite, for example, the work by Bloor and Ingham²⁷ who have carefully justified the use of an inviscid approach to obtain a leading-order approximation for their problem. One may also cite the corroborating numerical simulations reported by Hsieh and Rajamani,²⁸ Hoekstra, Derksen and Van den Akker,²⁹ Derksen and Van den Akker,³⁰ and others.

While the azimuthal flow behavior near the walls does not constitute a serious concern, it does pose a problem as the chamber axis is approached. Since u_θ becomes unbounded as $r \rightarrow 0$, the assumption of a free vortex is invalidated near the core. By analogy with unidirectional flow studies involving swirling motions, one may anticipate a forced vortex in the core region where viscous effects become appreciable. Recognizing that only numerical or asymptotic solutions are capable of elucidating the viscous core details, these will be fully explored in a forthcoming study.

K. Chamber Pressure

The radial pressure variation at the chamber head end is illustrated in Fig. 8a. Pressure variations in the axial direction are small and virtually indistinguishable from the trends observed at the head end. The head end is chosen because most of the available pressure measurements in the corresponding experiment are acquired at that location. As per Eq. (61), the parabolic decrease in the axial direction is negligible by comparison with radial variations. In practice ($l \geq 1$ and $\sigma \geq 10$), κ is so small that the pressure variation may be accurately approximated by $\Delta p \cong -1/(2r^2)$ independently of l and σ .

According to Eq. (57), the radial pressure gradient is independent of z . This trend is consistent with the behavior of the companion radial velocity. As illustrated in Fig. 8b, the radial pressure gradient is flat near the wall and steep near the core. In the vicinity of the core, a rapid rise in the pressure gradient is observed. The trend depicted in Fig. 8b is, in fact, consistent with recent cold-flow data acquired by Chiaverini and co-workers.³⁴ Practically, it can be seen from Eq. (57) that $\partial p/\partial r \cong 1/r^3$ is nearly insensitive to l and σ .

The axial pressure gradient, given by Eq. (58), is plotted in Fig. 8b. In addition to being independent of the radial coordinate, it only varies linearly with the distance from the head end. The small rate of diminution observed in Fig. 8c confirms the slow pressure depreciation in the axial direction. Note that $\partial p/\partial z = -z/(\sigma^2 l^2)$ decreases quadratically with l and σ .

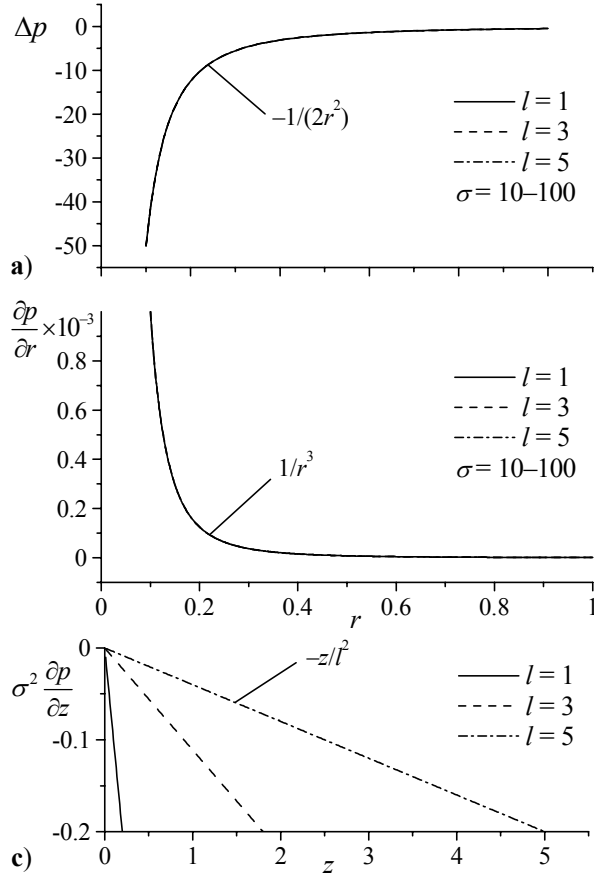


Fig. 8 Variation of a) the head-end chamber pressure and b) its gradient in the radial direction. Also shown in c) is the distribution of the axial pressure gradient along the length of the chamber.

L. Chamber Vorticity

In order to quantify the rotationality of the flow, it is instructive to evaluate the vorticity distribution in the chamber. Here the vorticity has an azimuthal component only. This result may be attributed to the flowfield being axisymmetric and to the radial and tangential velocities being independent of z . Based on Eqs. (23) and (56), one can write

$$\Omega_\theta = 4\pi^2 \kappa r z \sin(\pi r^2) = 2\pi r z \sin(\pi r^2) / (\sigma l) \quad (69)$$

Figure 9 illustrates the vorticity distribution along the chamber cross section at several axial stations. While the magnitude of Ω_θ increases linearly along the chamber length, it peaks at a radial position somewhere between the mantle and the wall. Based on Eq. (69), one can calculate the position corresponding to maximum vorticity from the root of

$$\tan(\pi r_{\max}^2) + 2\pi r_{\max}^2 = 0 \quad (70)$$

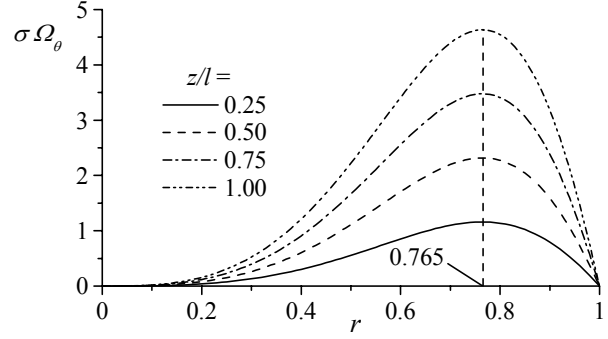


Fig. 9 Radial variation of chamber vorticity at several axial stations.

Numerically, one finds $r_{\max} \cong 0.764596$. This enables us to estimate the largest value of vorticity to be

$$\Omega_\theta(r_{\max}, z) \cong 29.12502 z \kappa = 4.63539 z / (\sigma l) \quad (71)$$

A maximum of $\Omega_{\max} \cong 4.63539 / \sigma$ is realized at $z = l$.

M. Swirl Intensity

Following Chang and Dhir,³⁵ the swirling intensity for a unidirectional vortex in a pipe of radius a and mean velocity u_m is given by

$$\tilde{Q} = \frac{2\pi \int_0^a \rho u_z u_\theta r dr}{\rho (\pi a^2) u_m^2} \quad (72)$$

Adapting this relation to the problem at hand requires integrating across the outlet flow cross section. The swirling intensity of the flow approaching the outlet may hence be calculated from

$$\tilde{Q} = 4u_m^{-2} \int_0^{1/\sqrt{2}} u_z u_\theta r dr \quad (73)$$

where the mean velocity must be averaged over the nozzle's base area A_b using

$$u_m = A_b^{-1} \iint_{A_b} \mathbf{u} \cdot \hat{\mathbf{n}} dA \quad (74)$$

Realizing that $\hat{\mathbf{n}} = \mathbf{e}_z$, one can proceed to write

$$\begin{aligned} u_m &= (2/\pi) \int_0^{2\pi} d\theta \int_0^{1/\sqrt{2}} u_z r dr \\ &= 8\pi \kappa z \int_0^{1/\sqrt{2}} \cos(\pi r^2) r dr = 4\kappa z = 2z / (\pi \sigma l) \end{aligned} \quad (75)$$

Subsequently, one obtains

$$\begin{aligned} \tilde{Q} &= \frac{4}{u_m^2} \int_0^{1/\sqrt{2}} u_z u_\theta r dr = \frac{\pi}{2\kappa z} \int_0^{1/\sqrt{2}} \cos(\pi r^2) dr \\ &= \frac{\pi}{2\sqrt{2}} \frac{C(1)}{\kappa z} = \frac{\pi^2}{\sqrt{2}} \frac{C(1)}{(z/l)} \sigma = \frac{\pi C(1)}{(z/l)} S \end{aligned} \quad (76)$$

Here $C(x)$ is the Fresnel integral made popular in diffraction theory; it is given by

$$C(x) = \int_0^x \cos(\frac{1}{2}\pi r^2) dr = x - \frac{1}{40}\pi^2 x^5 + \frac{1}{3456}\pi^4 x^9 + O(x^{13}) \quad (77)$$

The swirl intensity can hence be calculated from

$$\tilde{Q} \cong \frac{0.866244}{\kappa z} = \frac{5.44277}{z} \sigma l = 2.45011 \frac{S}{(z/l)} \quad (78)$$

Clearly, \tilde{Q} is largest at the head end and decreases in the downstream direction. This result has important practical implications because it suggests the inception of high mixing rates near the head end. This effect is especially beneficial under reactive flow conditions involving fuel addition. The large swirl intensity that one can associate with the bidirectional vortex near $z = 0$ has the potential of providing an optimal reactive flow environment in which rapid burning and increased combustion efficiency can be achieved. We conclude that the bidirectional vortex is ideally suited for operation in combustion chambers equipped with head-end fuel injection.

VI. Conclusions

Many past investigations have considered the bidirectional flow of a cyclone. While most of these studies have been experimental or numerical in nature, analytical solutions have been largely limited to semi-empirical or momentum-integral formulations. In this article, we have presented an exact solution of the Euler equations appropriate of a bidirectional vortex chamber that resembles an inverted cyclone separator. The current application arises in the context of a liquid oxidizer being injected tangentially into a thrust chamber. Nonetheless, the resulting flowfield remains applicable to a cylindrical cyclone with a flat base.

The inviscid flowfield derived here exhibits the fundamental characteristics observed in past and recent laboratory experiments. It also appears to agree quite favorably with recent computational work. Based on the inviscid solution, streamline patterns that bear a striking resemblance to those observed by other investigators are now available. The advent of an exact solution to this problem dispels the skepticism raised in the past regarding the possible establishment of a bipolar flow. In addition to providing a rigorous proof of existence, the analytical solution enables us to characterize several key features associated with this problem. For example, the location of the mantle separating the outer and inner vortex tubes is affirmed to be $1/\sqrt{2}$ or 71% of the chamber radius, a . Former experimental and numerical findings appear to converge over this value despite their reliance on averages or regression fits.

Consistent with former speculations, the radial velocity is found to be relatively smaller than the axial speed except near the head end where flow turning

requires a larger radial component. As predicted by recent numerical simulations, the maximum radial velocity is reached at $r \cong 0.61$. Along the length of the chamber, a radial cross flow, albeit small, is seen to exist between the outer and inner vortex tubes. The presence of cross flow is also confirmed by former tests and recent computational studies. Mean flow vorticity, on the other hand, reaches its peak value between the mantle and the wall at $r \cong 0.76$.

While vorticity increases linearly with the distance from the head end, we find the swirl intensity of the inner vortex to depreciate linearly as the nozzle is approached. In similar fashion, we find the pressure to depreciate slowly though quadratically with the distance from the head end. The corresponding pressure gradient, $\partial p/\partial z = -z/(\sigma^2 l^2)$, is slower in longer chambers or in chambers with higher swirl numbers. The axial rate of depreciation is virtually insignificant by comparison with the radial rate given by $1/r^3$. The radial depreciation is far more significant to the extent that one may write, $\Delta p \cong -1/(2r^2)$. Clearly, the net pressure drop increases with the injection velocity and the distance from the sidewall. The same can be said of the swirl velocity which becomes larger as the injection area ratio is decreased or as the distance from the sidewall is increased.

Due to the absence of viscous damping near the core, the swirl velocity continues to increase until it becomes unbounded at the chamber axis. This discontinuity is due to the inability of an inviscid model to capture the viscous core interactions that become significant near $r = 0$. The deficiency near the core does not undermine the predictive capabilities elsewhere. Nonetheless, an asymptotic analysis that accounts for the viscous corrections will be needed. Such treatment will be deferred to a later article.

Table 2 Comparison of the bidirectional vortex and the injection-driven profile by Culick (1966)

Injection-driven flow: Solid rocket motor	Swirl-driven flow: Liquid thrust chamber
$\mathbf{u} = u_r \mathbf{e}_r + u_z \mathbf{e}_z$	$\mathbf{u} = u_r \mathbf{e}_r + u_\theta \mathbf{e}_\theta + u_z \mathbf{e}_z$
$u_r = -\sin(\frac{1}{2}\pi r^2)/r$	$u_r = -\kappa \sin(\pi r^2)/r$
$u_\theta = 0$	$u_\theta = 1/r$
$u_z = \pi z \cos(\frac{1}{2}\pi r^2)$	$u_z = 2\pi \kappa z \cos(\pi r^2)$
$\boldsymbol{\Omega} = \pi^2 r z \sin(\frac{1}{2}\pi r^2) \mathbf{e}_\theta$	$\boldsymbol{\Omega} = 4\pi^2 \kappa r z \sin(\pi r^2) \mathbf{e}_\theta$
$\psi = z \sin(\frac{1}{2}\pi r^2)$	$\psi = \kappa z \sin(\pi r^2)$

The mean flow solution obtained in this study is reminiscent of Culick's injection-driven velocity profile³³ used to describe the bulk gas motion inside an idealized solid rocket motor chamber with circular cross section. The difference here lies in the presence of a swirl velocity component (see Table 2). The significance of the current solution in elucidating the technical aspects associated with bidirectional flows may be paralleled to that of Culick's in describing the core flow dynamics inside solid propellant rocket motors.

Inspired by Culick's profile and its relevance to theoretical studies of core flow motions in solid rocket motors, it may be desirable to study the stability of the bidirectional vortex to spatial and temporal disturbances inside vortex-driven liquid rocket engines. One may also wish to investigate the mechanisms of vortex precession and breakdown which have received much attention in the treatment of unidirectional flows. Also of interest will be the assessment of particle-mean flow damping triggered by the use of metal additives. While the heat transfer characteristics of the bipolar vortex are not yet studied, the hydrodynamic transition from a laminar to a turbulent regime remains an important problem in its own right, namely, one requiring further exploration. For these reasons, it is hoped that the current results will be used to open up additional lines of research inquiry.

Acknowledgments

The first two authors gratefully acknowledge the support received from NASA and the Wisconsin Space Grant Consortium. We are especially thankful for the direction and management of R. Aileen Yingst, Sharon D. Brandt, Steven I. Dutch, and Thomas H. Achtor. The authors also wish to thank William H. Knuth, Ronald R. Teeter, and Eric E. Rice of Orbital Technologies Corporation; their additional support is greatly appreciated.

References

- ¹Penner, S. S., "Elementary Considerations of the Fluid Mechanics of Tornadoes and Hurricanes," *Acta Astronautica*, Vol. 17, 1972, pp. 351-362.
- ²Königl, A., "Stellar and Galactic Jets: Theoretical Issues," *Canadian Journal of Physics*, Vol. 64, 1986, pp. 362-368.
- ³Harvey, J. K., "Some Observations of the Vortex Breakdown Phenomenon," *Journal of Fluid Mechanics*, Vol. 14, 1962, pp. 585-592.

- ⁴Sarpkaya, T., "On Stationary and Travelling Vortex Breakdowns," *Journal of Fluid Mechanics*, Vol. 45, No. 3, 1971, pp. 545-559.

- ⁵Faler, J. H., and Leibovich, S., "Disrupted States of Vortex Flow and Vortex Breakdown," *Physics of Fluids*, Vol. 20, No. 9, 1977, pp. 1385-1400.

- ⁶Leibovich, S., "The Structure of Vortex Breakdown," *Annual Review of Fluid Mechanics*, Vol. 10, 1978, pp. 221-246.

- ⁷Leibovich, S., "Vortex Stability and Breakdown: Survey and Extension," *AIAA Journal*, Vol. 22, No. 9, 1984, pp. 1192-1206.

- ⁸Beran, P. S., and Culick, F. E. C., "The Role of Non-Uniqueness in the Development of Vortex Breakdown in Tubes," *Journal of Fluid Mechanics*, Vol. 242, 1992, pp. 491-527.

- ⁹Hall, M. G., "Vortex Breakdown," *Annual Review of Fluid Mechanics*, Vol. 4, 1972, pp. 195-218.

- ¹⁰Lilley, D. G., "Swirl Flows in Combustion: A Review," *AIAA Journal*, Vol. 15, No. 8, 1977, pp. 1063-1078.

- ¹¹Gupta, A. K., Lilley, D. G., and Syred, N., *Swirl Flows*, Abacus, Turnbridge Wells, UK, 1984.

- ¹²Durbin, M. D., Vangsness, M. D., Ballal, D. R., and Katta, V. R., "Study of Flame Stability in a Step-Swirl Combustor," *Journal of Engineering for Gas Turbines & Power-Transactions of the ASME*, Vol. 118, No. April, 1996, pp. 308-314.

- ¹³Paschereit, C. O., Gutmark, E., and Weisenstein, W., "Excitation of Thermoacoustic Instabilities by Interaction of Acoustics and Unstable Swirling Flow," *AIAA Journal*, Vol. 38, No. 6, 2000, pp. 1025-1034.

- ¹⁴Cooper, A. J., and Peake, N., "Propagation of Unsteady Disturbances in a Slowly Varying Duct with Mean Swirling Flow," *Journal of Fluid Mechanics*, Vol. 445, 2001, pp. 207-234.

- ¹⁵Borissov, A., Shtern, V., and Hussain, F., "Modeling Flow and Heat Transfer in Vortex Burners," *AIAA Journal*, Vol. 36, No. 9, 1998, pp. 1665-1670.

- ¹⁶Reydon, R. F., and Gauvin, W. H., "Theoretical and Experimental Studies of Confined Vortex Flow," *The Canadian Journal of Chemical Engineering*, Vol. 59, 1981, pp. 14-23.

- ¹⁷Love, W. L., and Park, C., "An Experiment on the Mhd-Driven Rotating Flow for a Gas Core Nuclear Rocket," *AIAA Journal*, Vol. 8, 1970, pp. 1377-1385.

- ¹⁸ter Linden, A. J., "Investigations into Cyclone Dust Collectors," *Proceedings of the Institution of Mechanical Engineers*, Vol. 160, 1949, pp. 233-251.
- ¹⁹Kelsall, D. F., "A Study of Motion of Solid Particles in a Hydraulic Cyclone," *Transactions of the Institution of Chemical Engineers*, Vol. 30, 1952, pp. 87-103.
- ²⁰Smith, J. L., "An Experimental Study of the Vortex in the Cyclone Separator," *Journal of Basic Engineering-Transactions of the ASME*, 1962, pp. 602-608.
- ²¹Smith, J. L., "An Analysis of the Vortex Flow in the Cyclone Separator," *Journal of Basic Engineering-Transactions of the ASME*, 1962, pp. 609-618.
- ²²Fontein, F. J., and Dijksman, C., *Recent Developments in Mineral Dressing*, Institution of Mining and Metallurgy, London, 1953, p. 229.
- ²³Bloor, M. I. G., and Ingham, D. B., "Theoretical Investigation of the Flow in a Conical Hydrocyclone," *Transactions of the Institution of Chemical Engineers*, Vol. 51, 1973, pp. 36-41.
- ²⁴Vatistas, G. H., Lin, S., and Kwok, C. K., "Theoretical and Experimental Studies on Vortex Chamber Flows," *AIAA Journal*, Vol. 24, No. 4, 1986, pp. 635-642.
- ²⁵Vatistas, G. H., Lin, S., and Kwok, C. K., "Reverse Flow Radius in Vortex Chambers," *AIAA Journal*, Vol. 24, No. 11, 1986, pp. 1872-1873.
- ²⁶Vatistas, G. H., "Tangential Velocity and Static Pressure Distributions in Vortex Chambers," *AIAA Journal*, Vol. 25, No. 8, 1987, pp. 1139-1140.
- ²⁷Bloor, M. I. G., and Ingham, D. B., "The Flow in Industrial Cyclones," *Journal of Fluid Mechanics*, Vol. 178, 1987, pp. 507-519.
- ²⁸Hsieh, K. T., and Rajamani, R. K., "Mathematical Model of the Hydrocyclone Based on Physics of Fluid Flow," *AIChE Journal*, Vol. 37, No. 5, 1991, pp. 735-746.
- ²⁹Hoekstra, A. J., Derksen, J. J., and Van den Akker, H. E. A., "An Experimental and Numerical Study of Turbulent Swirling Flow in Gas Cyclones," *Chemical Engineering Science*, Vol. 54, 1999, pp. 2055-2065.
- ³⁰Derksen, J. J., and Van den Akker, H. E. A., "Simulation of Vortex Core Precession in a Reverse-Flow Cyclone," *AIChE Journal*, Vol. 46, No. 7, 2000, pp. 1317-1331.
- ³¹Chiaverini, M. J., Malecki, M. J., Sauer, J. A., and Knuth, W. H., "Vortex Combustion Chamber Development for Future Liquid Rocket Engine Applications," AIAA Paper 2002-2149, 2002.
- ³²Szeri, A., and Holmes, P., "Nonlinear Stability of Axisymmetric Swirling Flows," *Philosophical Transactions of the Royal Society of London, Series A*, Vol. 326, 1988, pp. 327-354.
- ³³Culick, F. E. C., "Rotational Axisymmetric Mean Flow and Damping of Acoustic Waves in a Solid Propellant Rocket," *AIAA Journal*, Vol. 4, No. 8, 1966, pp. 1462-1464.
- ³⁴Chiaverini, M. J., Private communication, 2003.
- ³⁵Chang, F., and Dhir, V. K., "Mechanisms of Heat Transfer Enhancement and Slow Decay of Swirl in Tubes with Tangential Injection," *International Journal of Heat and Fluid Flow*, Vol. 16, No. 2, 1995, pp. 78-87.